Static and quasielastic properties of the spiral magnet $Ba_2CuGe_2O_7$ studied by neutron resonance spin echo spectroscopy and neutron Larmor labeling

S. Mühlbauer,[1,*] J. Kindervater,[2] and W. Häußler[1,2]

[1]*Heinz Maier-Leibnitz Zentrum (MLZ), Technische Universität München, D-85748 Garching, Germany*

[2]*Physikdepartment, Technische Universität München, D-85748 Garching, Germany*

(Received 30 January 2015; revised manuscript received 28 October 2015; published 4 December 2015)

We provide a route to use elastic and quasielastic neutron spin echo spectroscopy (Larmor labeling) for a unified approach to study both the static and dynamic properties of incommensurate magnetic structures with small propagation vectors. The archetypal noncentrosymmetric spiral magnet $Ba_2CuGe_2O_7$ serves as a model system for our study. We show how Larmor labeling can efficiently decouple instrumental wavelength resolution and effective-$\vec{Q}$ resolution and give high-precision access to the structural properties of the incommensurate domains of $Ba_2CuGe_2O_7$.

DOI: 10.1103/PhysRevB.92.224406 PACS number(s): 75.50.Ee, 78.70.Nx, 75.70.Tj

I. INTRODUCTION

The structural and dynamical properties of spiral magnetic structures have raised a great deal of scientific interest in recent years. Skyrmion states have been identified in increasing number in bulk materials [1–7] and on surfaces and interfaces [8,9], indicating that they represent a general phenomenon not limited to the B20 family. Also, the particularly strong multiferroic properties of spiral magnets have been recognized by theory [10,11] and confirmed by experiments [12–14]. In addition to the multiferroic and topological properties of such materials, the phase transition into the spiral magnetic phase may also be of special interest [15]. If critical magnetic fluctuations soften at finite momentum transfer, they may assume enough phase space to significantly alter the properties of an otherwise second-order phase transition. This scenario, predicted by Brazovskii [16] for incommensurate magnetic structures in general, has recently been identified in the archetypal helimagnet MnSi [17,18]. Exclusively based on phase-space considerations, it is an interesting open question whether it is also applicable to systems with lower dimension.

In this paper, we show via a textbook experiment how neutron Larmor labeling on a neutron spin echo spectrometer can be used for a high-precision measurement of both the static and dynamic properties of incommensurate (spiral) magnetic structures beyond the resolution of a typical neutron diffractometer or triple-axis instrument. The noncentrosymmetric tetragonal antiferromagnet (AF) $Ba_2CuGe_2O_7$ ($P\bar{4}2_1m$) serves as a typical model system for our study. $Ba_2CuGe_2O_7$ shows an incommensurate spiral magnetic structure, provided by Dzyaloshinskii-Moryia (DM) [19,20] interaction. The basic feature of $Ba_2CuGe_2O_7$ is a square arrangement of Cu^{2+} ions in the (a,b) plane where nearest-neighbor AF exchange along the diagonal of the (a,b) plane is the dominant magnetic exchange. The coupling between adjacent planes is weakly ferromagnetic, leading to an effectively two-dimensional (2D) behavior. A schematic depiction of the unit cell of $Ba_2CuGe_2O_7$ together with the orientation of both DM vectors $\boldsymbol{D}_y$ and $\boldsymbol{D}_z$ is given in Fig. 1 of Ref. [21]. Below $T_N \approx 3.2$ K and at zero magnetic field, neutron diffraction has established an incommensurate, almost AF cycloidal magnetic structure in the (a,b) plane with $\xi = 0.0273$. Four magnetic satellite reflections indicative of two degenerate magnetic domains are thus observed at $(1 \pm \xi, \pm \xi, 0)$, centered at the AF Néel point (1,0,0) [21–26]. The phase transition from paramagnetism to spiral long-range order is characterized by an interplay of 2D physics and Brazovskii correlations [21,27]. In a magnetic field, $Ba_2CuGe_2O_7$ exhibits a multitude of different incommensurate magnetic structures, which suggest weak FM behavior and weak ferroelectricity [28]. For a detailed description, we refer the reader to [21,26,29].

The structure of the paper is as follows: In the first part, we theoretically consider the general case of elastic and quasielastic neutron spin echo measurements from incommensurate helical, cycloidal, and elliptical magnetic structures. As the resolution in $\vec{Q}$ space of a typical neutron spin echo spectrometer is limited by the velocity selector mostly used on such instruments, we consider in particular the interference effects that arise due to the overlap of multiple incommensurate domains. A characteristic beating of the spin echo signal as a function of precession field is expected by theory. This beating allows us efficiently to decouple the instrumental wavelength resolution and the effective-$\vec{Q}$ resolution, and it gives highly precise access to the structural properties of incommensurate domains. In the second part, we apply our theoretical findings to the special case of the almost AF cycloids in $Ba_2CuGe_2O_7$, where we accurately confirm our theoretical approach via our experiment on RESEDA operated by TUM at MLZ. We finally focus on quasielastic measurements of the linewidth of the diffraction peaks associated with the cycloidal spin spiral of $Ba_2CuGe_2O_7$, where we find the first hints of a broadening of the linewidth at T_N associated with the decay of the cycloidal magnetic order upon crossing T_N, whereas below T_N no dynamic processes are observed.

II. THEORY: SPIN ECHO AND SPIN ROTATION SIGNALS FROM MULTIPLE SPIRAL MAGNETIC DOMAINS

In this section, we theoretically examine how elastic neutron *spin rotation* (Larmor labeling) and quasielastic neutron *spin echo* measurements can be utilized for high-precision measurements of incommensurate magnetic structures with

*sebastian.muehlbauer@frm2.tum.de

long wavelengths on an atomic scale. The hallmark of such incommensurate magnetic structures is the existence of pairs of satellite reflections $(\pm k + G)$ with their propagation vector $k \ll G$ and the AF or FM zone center G, respectively. Due to the finite resolution in reciprocal space of any type of standard diffractometer or triple-axis spectrometer, it can be challenging to resolve these reflections. Therefore, we consider in particular effects that arise due to the overlap of such magnetic reflections.

A. Spin rotation signals from samples with a spin-dependent cross section

In spin echo measurements, the incoming neutron beam is polarized perpendicularly to the magnetic field direction in the primary and secondary spectrometer arm before and after the sample, respectively. Neutron spin precession takes place depending on the magnetic-field integral values in these regions, J_1 and J_2. Note that for the following paragraphs, we first consider only elastic scattering of the neutrons at the sample, hence no inelastic or quasielastic effects are taken into account.

We first focus on sample systems exhibiting a spin-dependent scattering cross section, therefore acting as neutron spin polarizers or analyzers of the scattered neutrons. For this purpose, we consider a sample with a helical spin structure such as the noncentrosymmetric helimagnet MnSi [30,31], which polarizes the neutron beam along the propagation vector of its helical spin structure. We assume a single domain state of the sample for our considerations. We first restrict ourselves to small values of J_1 and an arbitrarily large value of $J_2 \gg J_1$. Varying J_1 from zero to small values, the neutron spin phase ϕ_1 changes according to

$$\phi_1 = \frac{\gamma J_1}{h/(m_n/\lambda)}, \tag{1}$$

where γ is the neutron gyromagnetic ratio and $h/(m_n/\lambda)$ is the velocity if a neutron with mass m_n and wavelength λ.

The spin state is analyzed by the scattering process at the sample, leading to an oscillation of the intensity I in the scattered beam as a function of J_1,

$$I(J_1) = I_0(1 + \langle \cos \phi_1 \rangle), \tag{2}$$

with $I = I_0(1 + p)$ and the mean intensity I_0. The angular brackets denote the average over all neutron wavelengths contained in the neutron beam. Panel (a) of Fig. 1 shows the result theoretically expected of such a spin rotation measurement. The scan parameter J_1 is determined by the current value in the spin echo coils. Each J_1 step corresponds to a distinct value of the spin phase, with the sample serving as a spin analyzer. With increasing J_1, the intensity oscillates and its envelope decreases until the oscillations are wiped out when the spin phase of neutrons with different λ differs significantly more than 2π. This characteristic signal is denoted as a *spin rotation group*. The envelope of the spin rotation group is given by the Fourier transform of the wavelength distribution of the detected neutrons, and the frequency of the oscillations is given by the wavelength of the scattered neutrons. In Fig. 1, we assume a triangular distribution function of full width at half-maximum (FWHM) (1%), as typically approximatively

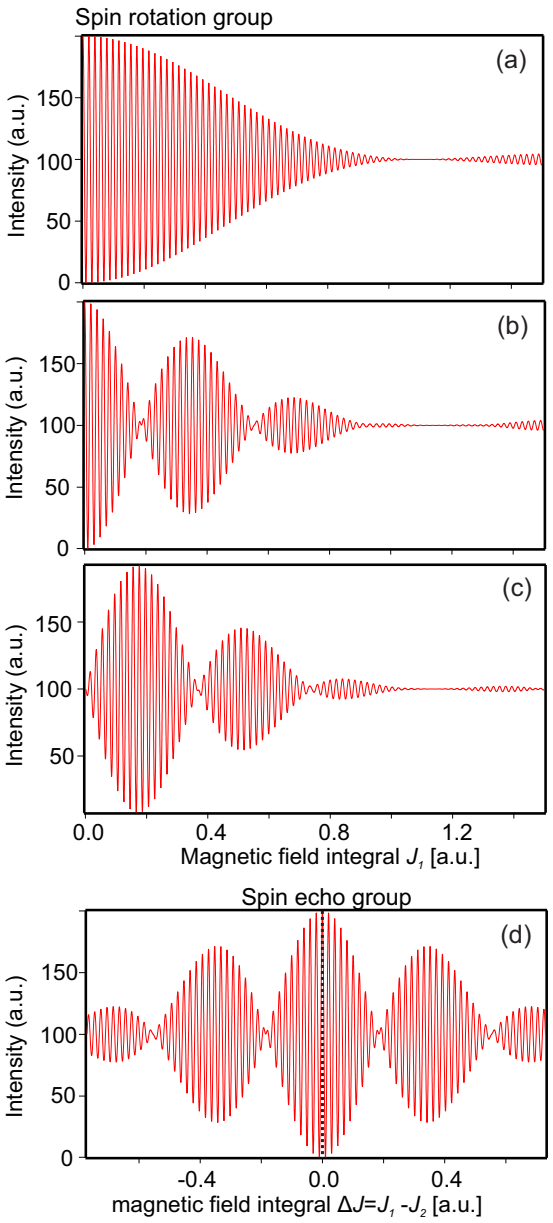

FIG. 1. (Color online) Panels (a)–(c) show the spin rotation group, theoretically expected for samples with a spin-dependent scattering cross section. For panel (a), a single helimagnetic domain was considered. For panels (b) and (c), the spin rotation group is the result of an overlap of two different helical domains with different propagation vectors with similar sign [panel (a)] and opposite sign [panel (c)]. Panel (d) shows spin echo for two overlapping magnetic domains.

resulting from the incoming wavelength spectrum convoluted with the mosaicity of a single crystalline sample and the divergence of the neutron beam. The spin rotation group does not depend on J_2 with $J_2 \gg J_1$: If J_2 is sufficiently large, the spin polarization created by the scattering process at the sample is reduced to zero during precession in J_2 between the sample and the spin analyzer in the secondary spectrometer arm. Consequently, the impact of the spin analyzer after J_2 restricts itself to halving the intensity of the scattered neutron beam.

It is worth noting that the limitation for the samples with polarizing properties can be avoided by the installation of an additional neutron polarizer after the sample region. The results of the above calculations remain intact, thus our considerations are valid for all incommensurate structures with small propagation vectors in general. However, tight technical restrictions apply to the neutron polarizer used for this purpose, as the flight path of the neutrons must not be affected.

B. Spin rotation signals from multiple overlapping incommensurate domains

As a second step, we now consider the general case of $S(\vec{Q})$ showing *two* distinct narrow maxima. It is irrelevant for our consideration if both satellite reflections represent two different incommensurate domains with different propagation vectors k_1 and k_2, or if they stem from a pair of incommensurate satellites at $(\pm k + G)$. Multi-k single domain and multidomain single k scenarios lead to identical results. Again, we assume polarizing properties for both maxima. In this case, the sample cuts out two distinct neutron wavelength and velocity bands, respectively. As already introduced, we compute the expected spin rotation group that results due to an overlap of both spiral propagation vectors k_1 and k_2. The envelope of the spin rotation group is then determined by both the incoming neutron spectrum and $S(\vec{Q})$, leading to

$$p(J_1) = \int_{\lambda_{k_1}} \cos\phi_1 d\lambda + \int_{\lambda_{k_2}} \cos\phi_1 d\lambda. \tag{3}$$

The existence of two different neutron velocities leads to a characteristic *interference* pattern between the two spin rotation groups, as shown in panel (b) of Fig. 1. In the case in which both helical or spiral domains contribute to the scattered intensity but with opposite polarization direction caused by a different handedness of the magnetic structure, the sign of one of the interfering components is reverted and the envelope function of the spin rotation group starts at zero, as shown in panel (c) of Fig. 1. In general, our case may be extended straightforwardly to more than two overlapping incommensurate satellite reflections.

C. Spin rotation signals from cycloidal magnetic domains

In this subsection, we consider in detail the signal expected for incommensurate cycloidal domains as found in $Ba_2CuGe_2O_7$. Due to the selection rules for magnetic neutron scattering, only the projection of the magnetization $\hat{\mathbf{M}}_\perp$ on a plane perpendicular to the momentum transfer $\vec{Q}$ contributes to the differential scattering cross section $d\sigma/d\Omega \propto |\langle\Psi_f|\hat{\mathbf{S}}\hat{\mathbf{M}}_\perp|\Psi_i\rangle|^2$ with the neutron spin operator $\hat{\mathbf{S}}$.

We assume localized magnetic moments at the lattice positions $\vec{G}_i$, and we introduce the continuous function $\Phi_\perp$ describing the direction of $\hat{\mathbf{M}}_\perp$. Then the matrix element reads

$$\frac{d\sigma}{d\Omega} \propto \left| \langle s_f | \int \hat{\mathbf{S}} \sum_{\vec{G}_j} \Phi_\perp(\vec{r}) \delta(\vec{r} - \vec{G}_j) e^{i\vec{Q}\cdot\vec{r}} d\vec{r} | s_i \rangle \right|^2, \tag{4}$$

where s_i and s_f are the initial and final spin functions, and the integral over the spatial planar wave functions has been carried out.

It is advantageous to choose the z axis of the Cartesian coordinate system pointing parallel to the momentum transfer $\vec{Q}$. The direction of the cycloidal magnetic moments with respect to $\vec{Q}$ is described by $\Phi = \hat{\mathbf{T}}(\cos\vec{k}\cdot\vec{r}, 0, \sin\vec{k}\cdot\vec{r})$, where $\vec{k}$ is the propagation vector of the cycloidal spin structure and α is the angle enclosed by the scattering plane and the plane of spin rotation, rotated by $\hat{\mathbf{T}}$. $\vec{k}$ is enclosed in the plane spanned by $\vec{Q}$ and the normal vector to the scattering plane. It is instructive to consider two special cases: For $\alpha = 0$, $\vec{k}$ is parallel to $\vec{Q}$ and $\Phi_\perp = (\cos\vec{k}\cdot\vec{r}, 0, 0)$. This corresponds just to a cosine modulated scattering potential leading to scattering without the creation of polarization. Otherwise, if $\alpha = 90^\circ$, $\vec{k}$ is orthogonal to $\vec{Q}$ so that scattering is found at out-of-plane positions above reciprocal-lattice vectors. In the general case,

$$\Phi = \begin{pmatrix} \cos\vec{k}\cdot\vec{r} \\ \sin\alpha\sin\vec{k}\cdot\vec{r} \\ \cos\alpha\sin\vec{k}\cdot\vec{r} \end{pmatrix}, \quad \Phi_\perp = \begin{pmatrix} \cos\vec{k}\cdot\vec{r} \\ \sin\alpha\sin\vec{k}\cdot\vec{r} \\ 0 \end{pmatrix} \tag{5}$$

and

$$\vec{k} = \hat{\mathbf{T}}\begin{pmatrix} 0 \\ 0 \\ 1 \end{pmatrix} = \begin{pmatrix} 0 \\ \sin\alpha \\ \cos\alpha \end{pmatrix}. \tag{6}$$

We hence find for these projected moments an effective elliptical magnetic structure, which can be decomposed in a circular helix and an amplitude modulation. Rewriting $a = \sin\alpha$ with the real number a, the operator of the matrix element of Eq. (4) reads

$$\hat{\mathbf{S}}\hat{\Phi}_\perp = \begin{pmatrix} 0 & (1+a)e^{i\vec{k}\cdot\vec{r}} + (1-a)e^{-i\vec{k}\cdot\vec{r}} \\ (1-a)e^{i\vec{k}\cdot\vec{r}} + (+a)e^{-i\vec{k}\cdot\vec{r}} & 0 \end{pmatrix}. \tag{7}$$

The spin-dependent cross section follows as

$$\left(\frac{d\sigma}{d\Omega}(Q)\right)_{ud} \propto (1+a)^2, \quad \left(\frac{d\sigma}{d\Omega}(-Q)\right)_{ud} \propto (1-a)^2, \quad \left(\frac{d\sigma}{d\Omega}(Q)\right)_{du} \propto (1-a)^2, \quad \left(\frac{d\sigma}{d\Omega}(-Q)\right)_{du} \propto (1+a)^2, \tag{8}$$

and

$$\left(\frac{d\sigma}{d\Omega}(Q)\right)_{uu} = \left(\frac{d\sigma}{d\Omega}(Q)\right)_{dd} = 0. \tag{9}$$

The scattered neutrons are partly polarized with polarization p_α,

$$p_\alpha \equiv \frac{(uu+du)-(ud+dd)}{uu+du+ud+dd} = \frac{-2\sin\alpha}{1+\sin\alpha^2}. \tag{10}$$

In analogy to samples with a circular helix and consequently a complete polarization of the neutron beam, a cycloidal spin spiral leads—in most cases—to a partial polarization of the scattered neutrons. This depends of course on the relative orientation of the momentum transfer $\vec{Q}$, the propagation vectors $\vec{k}$, and the plane of spin rotation. We hence expect a spin rotation and spin echo signal with a cosine beating similar to a helical sample, however with reduced amplitude of the oscillations. The considerations made above for overlapping multiple domains remain valid of course.

D. Spin echo signal from two overlapping incommensurate domains

We have already introduced the idea that with a sufficiently broad wavelength distribution, a relaxed detector resolution and beam collimation, and finally a finite magnetic mosaic, the intensity scattered from both satellite reflections $S(Q) = \delta(\vec{Q}+\vec{k}) + \delta(\vec{Q}-\vec{k})$ reaches the detector. This was shown to lead to an expression for the intensity of the neutron spin rotation signal,

$$I(\vec{Q},J_1) = \frac{\overline{I}}{2}\Bigg(2 + p_\alpha \int_{k_1} \cos\Phi_1[\lambda(k_1)]d\lambda + p_{-\alpha}\int_{k_2}\cos\Phi_1[\lambda(k_2)]d\lambda\Bigg), \tag{11}$$

with the mean scattered intensity $\overline{I}$ and the polarization p_α as defined in the preceding subsection. Due to the neutron wavelength spread of scattered neutrons from real magnetic domains of a certain width in $\vec{k}$, the envelope of spin rotation groups was found to decrease with increasing J_1 until it is wiped out above a certain threshold value of J_1. Depending on the phase of the neutrons and due to the polarizing properties of the sample, the probability of scattering varies between 0 and 1. Only the neutrons scattered at the sample enter the second precession region J_2. The *spin echo group* results from precession and backprecession of these neutrons in both flight paths before the sample and after the sample, respectively. The neutron intensity behind the spin analyzer before the detector thus depends on both field integrals. In our spin echo experiment, the neutron intensity $I(\vec{Q},\Delta J)$ is measured by a variation of $J_1 = J_2 + \Delta J$ in the vicinity of the spin echo point. We find for the intensity

$$I(\vec{Q},J_1) = \frac{\overline{I}}{2}\Bigg(2 + p_1 \int_{k_1} \cos(\Phi_1 - \Phi_2)d\lambda + p_2\int_{k_2}\cos(\Phi_1-\Phi_2)d\lambda\Bigg), \tag{12}$$

where p_1 and p_2 denote the *partial* recovery of the initial polarization due to quasielastic scattering. As the wavelength shift caused by quasielastic scattering is small compared to the wavelength band from the sample, cosine oscillations with the same envelope as for the spin rotation group are observed. Finally, if both domains exhibit the same dynamical behavior and accept the same wavelength band, we find for the spin echo signal

$$I(\vec{Q},J_1) = \frac{\overline{I}}{2}\Bigg\{2 + p(J)\Bigg[\int_{k_1}\cos\left(\frac{\gamma\lambda\Delta J}{h/m}\right)f(\lambda-\lambda_1)d\lambda + \int_{k_2}\cos\left(\frac{\gamma\lambda\Delta J}{h/m}\right)f(\lambda-\lambda_2)d\lambda\Bigg]\Bigg\}. \tag{13}$$

A typical spin echo curve is visualized in panel (d) of Fig. 1. It is important to note that in contrast to the spin rotation group, no clear prediction on the symmetry of the envelope function of the cosine oscillations can be made based on the polarization direction of the overlapping domains. This is caused by differences of the spin phase between neutrons scattered in slightly different scattering angles moving on slightly different trajectories [32], which are in turn caused by the finite collimation of the beam and the finite mosaicity of the sample.

To conclude, we have computed the interference effects that arise in the *spin rotation group* and *spin echo group* due to the presence of multiple incommensurate satellite reflections with polarizing properties. We showed how these interference effects can be utilized straightforwardly for a highest precision measurement of the structural magnetic properties of the sample. This method is denoted *neutron Larmor labeling*. Again, as in the first part of this section, similar results could be obtained using a polarizer after the sample region instead of samples with polarizing properties.

Note that up to now we have considered quasielastic effects only by introducing the constants p_1 and p_2, which denote the recovery of the quasielastic polarization. For a measurement of the quasielastic linewidth, the spin echo is recorded for different values of J_1 and $J_1 = J_2 + \Delta J$, hence different spin echo times τ. The decay of the spin echo signal for increasing τ is either normalized to the same sample at very low temperature, where no quasielastic broadening is expected, or to a different sample with known strictly elastic properties such as graphite or vanadium. The decay is then fitted to an exponential decay with the characteristic quasielastic linewidth Γ.

III. STATIC AND QUASIELASTIC PROPERTIES OF THE CYCLOIDAL MAGNETIC STRUCTURE OF $Ba_2CuGe_2O_7$

A. Experimental methods

We apply our findings to the special case of $Ba_2CuGe_2O_7$ and compare the results of the theoretical considerations to our experiment on the neutron resonance spin echo spectrometer RESEDA. For this purpose, a single crystal with a diameter of ∼5 mm and a length of ∼19 mm has been used. This crystal has already been utilized in several neutron diffraction experiments; a detailed description of the growth and annealing process of the sample is given in Ref. [21]. The sample has been mounted with the $(0,-1,0)$ crystalline direction vertical and then cooled by a closed cycle refrigerator with a third additional 1.5 K stage. Measurements have been taken in a temperature range between 1.65 and 4 K with a temperature stability of ±0.002 K. A sketch of the reciprocal space is shown in Fig. 2(a), where the area shaded in green represents the instrumental resolution. RESEDA was used with a neutron wavelength of $\lambda = 5.34$ Å, monochromatized by an

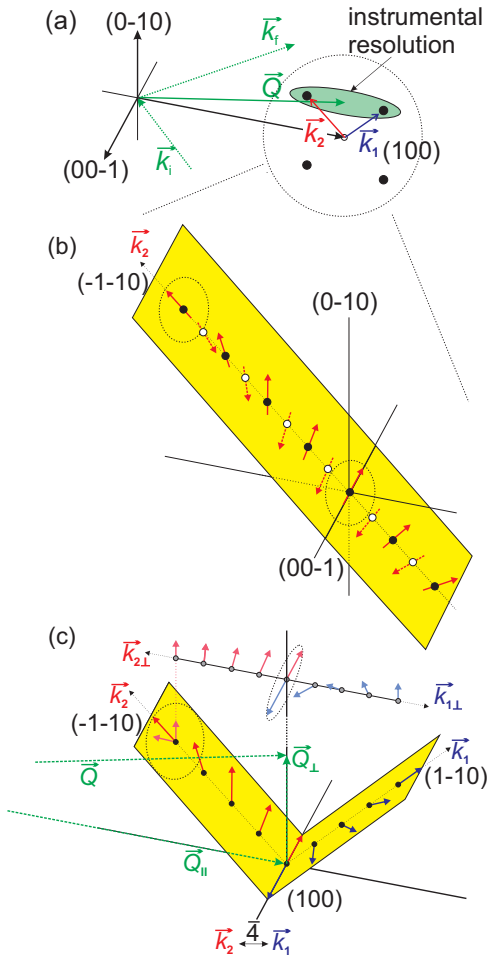

FIG. 2. (Color online) (a) Schematic depiction of the experimental setup with the $(0,-1,0)$ axis vertical. The momentum transfer $\vec{Q}$ is aligned almost parallel to (1,0,0) along $(1\pm\xi,\pm\xi,0)$. The instrumental resolution is given by the shaded green ellipsoid. (b) Illustration of the almost antiferromagnetic cycloidal magnetic structure of $Ba_2CuGe_2O_7$. Shown is the domain with its propagation vector $\vec{k}_2$ along $(-1,-1,0)$. Panel (c) depicts both cycloidal magnetic domains of $Ba_2CuGe_2O_7$ with propagation vectors $(\pm1,-1,0)$ in red and blue, respectively. For clarity, only one sublattice is drawn. Both domains are related by the symmetry operation $\bar{4}$. In addition, we show the projection of the staggered moments perpendicular to the momentum transfer $\vec{Q}$ in light red and blue with effective propagation vectors $\vec{k}_{1\perp}$ and $\vec{k}_{2\perp}$.

ASTRIUM mechanical velocity selector with a wavelength spread of 16%. A beam collimation of 30 mm and the length of the spectrometer arms of 3.95 m lead to a geometrical resolution of 0.51°. The sample has been aligned using strong nuclear (2,0,0) reflections.

The hallmark of the almost AF cycloidal magnetic structure of $Ba_2CuGe_2O_7$ [cf. panel (b) of Fig. 2] is four incommensurate satellite reflections at $(1\pm\xi,\pm\xi,0)$ centered at the Néel point. The two magnetic domains are denoted $\vec{k}_1=(1\pm\xi,\mp\xi,0)$ and $\vec{k}_2=(1\mp\xi,\pm\xi,0)$. Typical scans of the sample around the (1,0,0) peak position are shown in Fig. 3, illustrating the overlap of two pairs of incommensurate satellite reflections. In the case of $Ba_2CuGe_2O_7$, two satellite reflections of different domains overlap. Panel (a) shows a

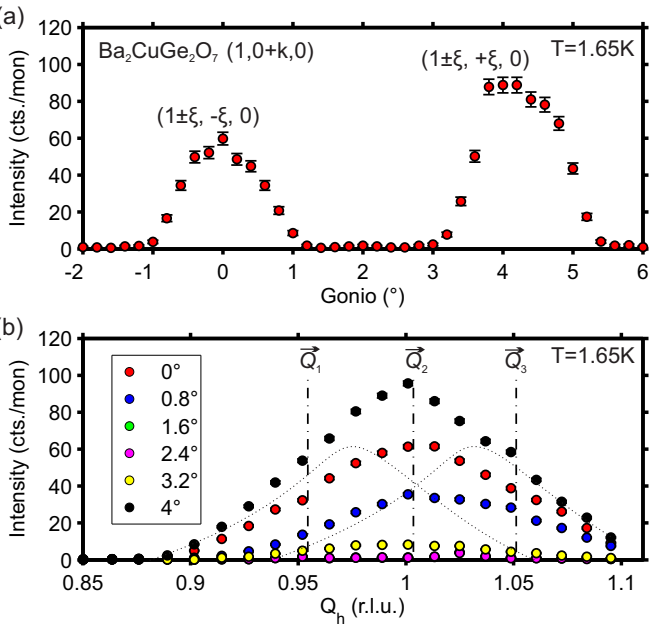

FIG. 3. (Color online) (a) Transverse **Q** scan along $(1,0+k,0)$ showing two peaks associated with the incommensurate satellite peaks at $(1\pm\xi,-\xi,0)$ and $(1\pm\xi,+\xi,0)$. (b) Longitudinal **Q** scan along $(h,0,0)$ for different goniometer angles. Here, both incommensurate satellites at $(1\pm\xi,-\xi,0)$ and $(1\pm\xi,+\xi,0)$ overlap due to the coarse instrumental resolution. The dotted line indicates both incommensurate satellites.

gonio-scan corresponding to a rotation around the $(0,0,-1)$ axis. The incommensurate satellite pairs at $(1\pm\xi,-\xi,0)$ and at $(1\pm\xi,+\xi,0)$ can be separated due to the tight collimation of the neutron beam. In contrast, panel (b) shows longitudinal $\vec{Q}$ scans along the $(h,0,0)$ direction for different gonio-angles. Here, the overlap of $(1\pm\xi,-\xi,0)$ and $(1\pm\xi,+\xi,0)$ is clearly visible.

Both cycloidal magnetic domains are connected by the symmetry operation $\bar{4}$, as schematically shown in Fig. 2(c). For better visibility, the staggered magnetization of the two almost AF sublattices is plotted in blue ($\vec{k}_1$) and red ($\vec{k}_2$). As the incommensurability is small ($\xi=0.0273$), $\vec{Q}$ is nearly parallel to (1,0,0) with $\alpha=45°$. The decomposition of the cycloidal magnetic structure of $Ba_2CuGe_2O_7$ according to Eq. (7) is illustrated in the upper part of panel (c), where the effective elliptical magnetic structure of the projected staggered moments is shown in light blue and red with an effective propagation vector ($\vec{k}_{1\perp}$) and ($\vec{k}_{2\perp}$) parallel to $\vec{Q}_\parallel$. The helicity of both domains is left-handed. As for an ideal helical modulation of spins, polarization is generated along $\vec{Q}$, opposite for $\pm\vec{k}$. For a single domain state of $Ba_2CuGe_2O_7$, we would therefore expect a spin rotation signal similar to panel (a) of Fig. 1, however with reduced amplitude. Due to the two overlapping incommensurate satellite reflections, we therefore expect a spin rotation signal similar to the one given in panel (c) of Fig. 1 and a spin echo signal as shown in panel (d).

For the measurements of the linewidth associated with the cycloidal magnetic structure of $Ba_2CuGe_2O_7$, the spin echo time τ has been varied between 0.08 and 1 ns, where data points below $\tau<0.4$ ns have been measured in a neutron

spin echo (NSE) setup, while points above 0.4 ns have been measured in neutron resonance spin echo (NRSE) mode. These measurements have been repeated for sample temperatures from 2.8 to 3.05 K.

B. Elastic measurements—Larmor labeling

We start with a description of the elastic signal contained in the *spin rotation* group and the *spin echo* group. All elastic data have been obtained at a temperature of $T = 1.65$ K. At this temperature, we assume that no intrinsic dynamical behavior is present in the sample; the neutrons are scattered elastically. This dataset is taken at a small spin echo time of 0.08 ns using the NSE setup of RESEDA. Three typical datasets are shown in Fig. 4, corresponding to positions $\vec{Q}_1$, $\vec{Q}_2$, and $\vec{Q}_3$, as indicated in Fig. 3. Both spin rotation and spin

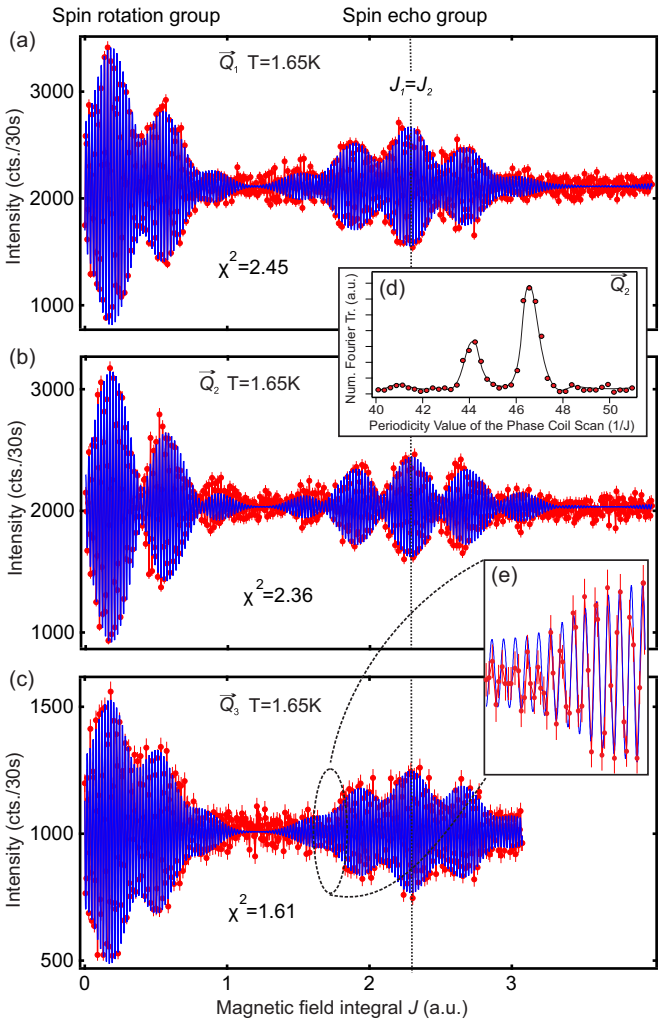

FIG. 4. (Color online) (a), (b), and (c) Elastic spin rotation signals and spin echo signals, recorded at a temperature of $T = 1.65$ K and for a spin echo time of $\tau = 0.08$ ns. The scans have been performed at positions $\vec{Q}_1$, $\vec{Q}_2$, and $\vec{Q}_3$ as indicated in Fig. 3. The red data points correspond to the measured points. The fitted model is shown in blue. The inset (d) shows the numerical Fourier transform of the spin rotation and spin echo group at $\vec{Q}_2$. Inset (e) depicts a zoomed version of the recorded data points and the corresponding fit function.

echo clearly show pronounced cosine oscillations. Moreover, the envelope of spin rotation and spin echo shows a pronounced beating, exactly as predicted by our theoretical model for the magnetic structure of $Ba_2CuGe_2O_7$. Note that due to a slight $\theta/2\theta$ mismatch, the absolute intensity of these scans does not correspond to the values of Fig. 3(b). The relative intensities from both domains are slightly modified, as will become clear below.

We fit the spin rotation and spin echo group for $\vec{Q}_1$, $\vec{Q}_2$, and $\vec{Q}_3$ using the equation

$$I(J) = I_0 + BSE^{\text{rot}} + BSE^{\text{echo}}, \tag{14}$$

where $BSE^{\text{rot}}(J)$ represents the spin rotation group, $BSE^{\text{echo}}(J)$ represents the echo group, and I_0 stands for a constant background signal. Spin echo and spin rotation group are hence fitted independently using

$$BSE^i(J) = A^i_{k1}\cos\left[\phi_{\text{sc}}\left(J - J^i_1\right)\right]\frac{\sin^2\left[\Delta_\lambda\phi_{\text{sc}}\left(J - J^i_2\right)\right]}{\Delta^2_\lambda(\phi_{\text{sc}})^2\left(J - J^i_2\right)^2} + A^i_{k2}\cos\left[\phi_{\text{sc}}\left(J - J^i_1\right)\right]\frac{\sin^2\left[\Delta_\lambda\phi_{\text{sc}}\left(J - J^i_2\right)\right]}{\Delta^2_\lambda(\phi_{\text{sc}})^2\left(J - J^i_2\right)^2} \tag{15}$$

with $i = (\text{echo,rot})$. The width of the wavelength band is denoted Δ_λ. The parameters A^{rot}_{k1} and A^{rot}_{k2} denote both amplitudes of the domains of the spin rotation group, while A^{echo}_{k1} and A^{echo}_{k2} denote both amplitudes for the echo group, respectively. The parameters J^{rot}_1 and J^{rot}_2 denote the center of the cosine oscillation and the center of the envelope function for the spin rotation group, similar for the echo group with J^{echo}_1 and J^{echo}_2, respectively. The spin phase per scan variable is denoted $\phi_{\text{sc}} = \frac{1}{v_n}L_{\text{NRSE}}$, and it connects the field integral with the velocity of the neutrons, which in turn assigns a fixed value in $\vec{Q}$ space with $\frac{1}{v_n} = \frac{4\pi}{Q}\sin\left(\frac{\pi}{360}2\theta\right)$.

Equation (15) is a result of an integration of Eq. (13) assuming triangular functions for the wavelength bands. The fits are included in Fig. 4 as solid blue lines. The excellent agreement of fit and data is illustrated in the inset panel (e). The results of the fits for $\vec{Q}_1$, $\vec{Q}_2$, and $\vec{Q}_3$ are summarized in Table I.

The fit indicates that the scattered neutrons consist of two wavelength fractions being separated by the factor $2k_{\text{rel}} = 2 \times 0.0268$ (r.l.u.), and it provides the amplitudes of both fractions corresponding to both domains. Despite an initial wavelength band of 16% width of the velocity selector, which leads to a full overlap of the incommensurate satellites, a highly precise measurement of the incommensurability is nevertheless possible with our method. The resolution of our method exceeds the resolution limits of typical triple-axis spectrometers or cold diffractometers by approximately one order of magnitude. Moreover, the spin rotation groups recorded for $Ba_2CuGe_2O_7$ precisely correspond to the theoretical model for two components with opposite polarization, as introduced in Fig. 2, panel (b).

We finally test our model for consistency. For this purpose, we compute the numerical Fourier transform of the spin rotation and spin echo data at $\vec{Q}_2$ as shown in the inset of Fig. 4(d). The Fourier transform unambiguously proves the

TABLE I. Fitting parameters for the spin rotation and spin echo signal for $\vec{Q}_1$, $\vec{Q}_2$, and $\vec{Q}_3$ at $T = 1.6$ K and $\tau = 0.08$ ns.

Variable	$\vec{Q}_1$	$\vec{Q}_2$	$\vec{Q}_3$
I_0 (cts/30 s)	2033.7 ± 1.7	2112.5 ± 1.7	1007 ± 1.4
A_{k1}^{rot} (cts/30 s)	497 ± 8	974 ± 10	404 ± 6
A_{k2}^{rot} (cts/30 s)	-656 ± 9	-371 ± 7	-118 ± 5
A_{k1}^{echo} (cts/30 s)	-162 ± 6	-404 ± 6	-54 ± 4
A_{k2}^{echo} (cts/30 s)	-255 ± 7	-169 ± 5	-189 ± 5
Δ_λ (10^{-3})	8.2 ± 0.15	8.7 ± 0.1	9 ± 0.2
Q_{Bragg} (Å^{-1})	0.7469	0.7469	0.7469
k_{rel} (r.l.u.)	$0.026\,75 \pm (8 \times 10^{-5})$	$0.027\,04 \pm (8 \times 10^{-5})$	$0.0259 \pm (2 \times 10^{-4})$

existence of two distinct values of the propagation vector for $\vec{Q}_2$ at $(1 \pm \xi, -\xi, 0)$. The Fourier transform of the data numerically validates the assumption of a triangular spectrum of the selector's wavelength band by the Bragg reflection at the sample. The estimated bandwidth selected by the scattering process at the sample yields 0.83% FWHM, calculated from the geometrical resolution of 0.51° with $\lambda = 4\pi/Q \sin(\theta)$ and $\Delta\lambda = 1/[2\tan(\theta)](\Delta\theta/\theta)$. The width of the fitted wavelength band of 0.9% is in good agreement. In fact, it is small compared to the wavelength band provided by the wavelength selector as the sample acts like a monochromator.

In conclusion, we have shown that detailed information on the high-precision structural properties of the magnetic spin cycloid of $Ba_2CuGe_2O_7$ can be extracted with the help of elastic spin rotation and spin echo signals (Larmor labeling) obtained on the spectrometer RESEDA, even though the $\vec{Q}$ resolution of RESEDA is not sufficient to resolve the different incommensurate peaks. Our method illustrates an alternative way to examine the growing collection of incommensurate spiral, helical, and cycloidal magnetic structures, where we efficiently decouple the instrumental wavelength resolution—and hence intensity—from the effective $\vec{Q}$ resolution. Our approach can be generalized to samples without polarizing properties by the installation of an additional neutron polarizer directly after the sample position, notably a 3He transmission polarizer, before entering the precession region of the secondary spectrometer arm. In related approaches, mode multiplets [33] and the distribution of lattice constants of single crystals [34] have been studied using NRSE.

C. Quasielastic measurements

In this subsection, we finally turn to the measurements of the quasielastic linewidth of the Bragg peaks upon crossing the paramagnetic to helimagnetic transition at T_N. The temperature dependence of the integrated intensity of the incommensurate spots is shown in the inset of Fig. 6. A transition temperature of $T_N = 3.05$ K was inferred from the integrated intensity. The quasielastic measurements were performed in a temperature range from 2.8 to 3.05 K. All data were fitted considering both the *spin rotation* and the *spin echo* group. The parameters for the spin rotation group were taken from Fig. 4. The amplitudes and the mean intensity were corrected for the temperature dependence shown in Fig. 6. All data are normalized to low-temperature data measured at $T = 1.65$ K. The resulting data for $S(q,\tau)/S(q,0)$ are shown in Fig. 5 as a function of spin echo time τ together with the fit function. The spread of the groups of data points comparing different spin echo times is mostly caused by the normalization process. A decay of the elastic signal observed for $T = 3.04$ K for increasing spin echo time can be seen, which is also reflected in the linewidth. To extract the quasielastic linewidth, a single exponential decay of the form

$$\frac{S(q,\tau)}{S(q,0)} = A \exp\left(\frac{-\Gamma\tau}{0.658\,21\ \mu\mathrm{eV}}\right) + y_0 \qquad (16)$$

with $y_0 = 0$ and $A = 1$ has been fitted to the data. The resulting linewidth obtained by the fits is plotted as a function of temperature in Fig. 6 together with the integrated intensity. As already seen, first indications of an increasing quasielastic linewidth Γ outside of the error bars can be observed in the range of 0.4 μeV very close to the transition temperature T_N at $T = 3.04$ K. However, due to the further decreasing intensity in this region and the correspondingly increasing error bars, this tendency could not be traced above the transition at T_c. In other studies on $Ba_2CuGe_2O_7$ using triple-axis spectroscopy (TAS) (Ref. [27]), a ring of intensity was observed in a finite-temperature interval of ≈0.5 K above the transition temperature T_N. As the vertical divergence accepted by TAS is considerably larger as compared to our setup, the area of integration in reciprocal space is smaller, making the ring feature very weak on RESEDA. The intensity recorded in this regime above T_c with dynamic correlations did not allow for spin echo measurements in a reasonable time scale. Our data are hence limited to temperatures $T \leqslant T_N$. For the same

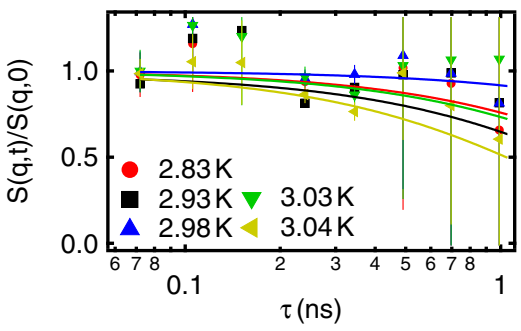

FIG. 5. (Color online) $S(q,\tau)/S(q,0)$ is shown as a function of the spin echo time τ for different sample temperatures closely below and at the transition temperature T_N.

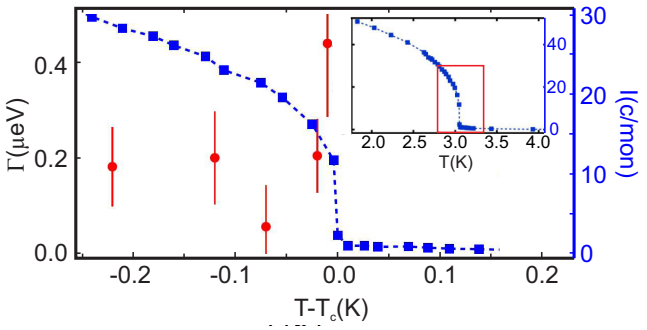

FIG. 6. (Color online) The blue symbols depict the temperature dependence of the integrated intensity of the incommensurate satellite reflections of $Ba_2CuGe_2O_7$ at $(1 \pm \xi, -\xi, 0)$. The inset shows the temperature dependence of the integrated intensity in a broader temperature range. The red markers indicate the quasielastic linewidth associated with the incommensurate satellite reflections as a function of temperature as obtained from the decay of the spin echo signal.

reason, the data are largely limited by the statistical error. A quantitative study of the temperature dependence of the linewidth above the transition temperature therefore remains a topic for future experiments.

IV. CONCLUSION

In our work, we have studied the properties of the noncentrosymmetric helimagnet $Ba_2CuGe_2O_7$ by means of neutron spin echo and neutron resonance spin echo spectroscopy. We have shown experimentally and theoretically that a characteristic beating of the *spin rotation* and *spin echo* signal, which is caused by the polarizing properties of the sample, allows for a precise measurement of the incommensurate propagation vectors that is otherwise inaccessible with the instrumental resolution. Our study illustrates a way to use this Larmor labeling technique on neutron spin echo spectrometers as a general approach for the investigation of the structural and quasielastic properties of incommensurate magnetic structures of different kinds.

ACKNOWLEDGMENTS

We wish to thank E. Pomjakushina, K. Conder, P. Böni, and N. Martin for support and stimulating discussions. Technical support and help from R. Bierbaum and P. Biber is gratefully acknowledged. J.K. acknowledges financial support from TUM Graduate School and ERC Advanced Grant No. 291079.

[1] S. Mühlbauer, B. Binz, F. Jonietz, C. Pfleiderer, P. Böni, A. Rosch, A. Neubauer, and R. Georgii, Science **323**, 915 (2009).
[2] X. Z. Yu, Y. Onose, N. Kanazawa, J. H. Park, J. H. Han, Y. Matsui, N. Nagaosa, and Y. Tokura, Nature (London) **465**, 901 (2010).
[3] C. Pfleiderer, T. Adams, A. Bauer, W. Biberacher, B. Binz, F. Birkelbach, P. Böni, C. Franz, R. Georgii, M. Janoschek *et al.*, J. Phys.: Condens. Matter **22**, 164207 (2010).
[4] F. Jonietz, S. Mühlbauer, C. Pfleiderer, A. Neubauer, W. Münzer, A. Bauer, T. Adams, R. Georgii, P. Böni, R. A. Duine *et al.*, Science **330**, 1648 (2010).
[5] W. Münzer, A. Neubauer, T. Adams, S. Mühlbauer, C. Franz, F. Jonietz, R. Georgii, P. Böni, B. Pedersen, M. Schmidt *et al.*, Phys. Rev. B **81**, 041203 (2010).
[6] X. Z. Yu, N. Kanazawa, Y. Onose, K. Kimoto, W. Z. Zhang, S. Isiwata, Y. Matsui, and Y. Tokura, Nat. Mater. **10**, 106 (2011).
[7] S. Seki, X. Z. Yu, S. Ishiwata, and Y. Tokura, Science **336**, 198 (2012).
[8] S. Heinze, K. von Bergmann, M. Menzel, J. Brede, A. Kubetzka, R. Wiesendanger, G. Bihlmayer, and S. Blügel, Nat. Phys. **7**, 713 (2011).
[9] N. Romming, C. Hanneken, M. Menzel, J. E. Bickel, B. Wolter, K. von Bergmann, A. Kubetzka, and R. Wiesendanger, Science **341**, 636 (2013).
[10] M. Mostovoy, Phys. Rev. Lett. **96**, 067601 (2006).
[11] I. A. Sergienko and E. Dagotto, Phys. Rev. B **73**, 094434 (2006).
[12] T. Kimura, G. Lawes, and A. P. Ramirez, Phys. Rev. Lett. **94**, 137201 (2005).
[13] M. Kenzelmann, A. B. Harris, S. Jonas, C. Broholm, J. Schefer, S. B. Kim, C. L. Zhang, S. W. Cheong, O. P. Vajk, and J. W. Lynn, Phys. Rev. Lett. **95**, 087206 (2005).
[14] G. Lawes, A. B. Harris, T. Kimura, N. Rogado, R. J. Cava, A. Aharony, O. Entin-Wohlman, T. Yildrim, M. Kenzelmann, C. Broholm, and A. P. Ramirez, Phys. Rev. Lett. **95**, 087205 (2005).
[15] H. Kawamura, J. Phys.: Condens. Matter **10**, 4707 (1998).
[16] S. A. Brazovskii, Sov. Phys. JETP **41**, 85 (1975).
[17] M. Janoschek, M. Garst, A. Bauer, P. Krautscheid, R. Georgii, P. Böni, and C. Pfleiderer, Phys. Rev. B **87**, 134407 (2013).
[18] J. Kindervater, W. Häußler, M. Janoschek, C. Pfleiderer, P. Böni, and M. Garst, Phys. Rev. B **89**, 180408 (2014).
[19] I. E. Dzyaloshinskii, J. Phys. Chem Solids **4**, 241 (1958).
[20] T. Moriya, Phys. Rev. **120**, 91 (1960).
[21] S. Mühlbauer, S. Gvasaliya, E. Ressouche, E. Pomjakushina, and A. Zheludev, Phys. Rev. B **86**, 024417 (2012).
[22] A. Zheludev, G. Shirane, Y. Sasago, N. Koide, and K. Uchinokura, Phys. Rev. B **54**, 15163 (1996).
[23] A. Zheludev, S. Maslov, G. Shirane, Y. Sasago, N. Koide, and K. Uchinokura, Phys. Rev. Lett. **78**, 4857 (1997).
[24] A. Zheludev, S. Maslov, G. Shirane, I. Tsukada, T. Masuda, K. Uchinokura, I. Zaliznyak, R. Erwin, and L. P. Regnault, Phys. Rev. B **59**, 11432 (1999).
[25] A. Zheludev, S. Maslov, G. Shirane, Y. Sasago, N. Koide, K. Uchinokura, D. A. Tennant, and S. E. Nagler, Phys. Rev. B **56**, 14006 (1997).
[26] S. Mühlbauer, S. N. Gvasaliya, E. Pomjakushina, and A. Zheludev, Phys. Rev. B **84**, 180406 (2011).
[27] S. Mühlbauer, G. Brandl, M. Mannson, and M. Garst (unpublished).
[28] H. Murakawa, Y. Onose, and Y. Tokura, Phys. Rev. Lett. **103**, 147201 (2009).

[29] J. Chovan, M. Marder, and N. Papanicolaou, Phys. Rev. B **88**, 064421 (2013).

[30] J. Kindervater, W. Häussler, A. Tischendorf, and P. Böni, J. Phys.: Conf. Ser. **340**, 012030 (2012).

[31] M. Janoschek, Ph.D. thesis, Technische Unitversität München (2008).

[32] F. Mezei, *Neutron Spin Echo*, Lecture Notes in Physics, Vol. 128 (Springer, Berlin, 1980).

[33] F. Groitl, K. Kiefer, and K. Habicht, Proceedings of the 8th International Workshop on Polarised Neutrons for Condensed Matter Investigation [Physica B **406**, 2342 (2011)].

[34] C. Pfleiderer, P. Böni, T. Keller, U. K. Rößler, and A. Rosch, Science **316**, 1871 (2007).